Optimal Approaches of Unmanned Helicopters in Wind-Sensitive Maritime Operations

Zilver, Damy; Varriale, Carmine; Pavel, Marilena; Voskuijl, Mark

DOI
10.4050/F-0081-2025-248

Publication date
2025

Document Version
Final published version

Citation (APA)
Zilver, D., Varriale, C., Pavel, M., & Voskuijl, M. (2025). *Optimal Approaches of Unmanned Helicopters in Wind-Sensitive Maritime Operations*. Paper presented at 81st Annual Vertical Flight Society Forum and Technology Display, FORUM 2025, Virginia Beach, United States. https://doi.org/10.4050/F-0081-2025-248

Optimal Approaches of Unmanned Helicopters in Wind-Sensitive Maritime Operations

Damy Zilver MSc. Student
Carmine Varriale Assistant Professor
Marilena Pavel Associate Professor
Delft University of Technology, Delft, The Netherlands

Mark Voskuijl
Full Professor
Netherlands Defense Academy, Den Helder, The Netherlands

ABSTRACT

Helicopters' Vertical Take-Off and Landing (VTOL) capabilities are essential for maritime operations, especially for small-deck naval vessels. Unmanned Aerial Vehicles (UAVs) offer a cheaper, expendable, and efficient alternative for certain tasks, such as reducing pilot risk and lowering fuel consumption. While the procedures to approach and land on (moving) ships are standardized and bound to established operational limits in the case of crewed helicopters, UAVs lack such guidelines. This study investigates optimal rotary-wing UAV approach trajectories to a moving ship, for varying wind conditions and relative initial positions, and for different objectives. The goal is to provide preliminary guidelines for maritime UAV recovery operations, and a preliminary estimation of performance-based operational limits. The optimal trajectories are obtained using a global path-performance optimization framework based on Optimal Control Theory. The trajectories are compared to each other and to reference cases using the Longest Common SubSequence (LCSS) similarity measure, revealing how the unmanned helicopter adjusts its path to exploit the wind direction and profile for more efficient ground speeds. The violation of performance and/or geometric constraints is used to preliminarily indicate the presence of operational boundaries. The control effort and energy consumption are used to identify optimal starting positions for the helicopter approach phase for a given wind profile and intensity.

NOTATION

c_d	Mean profile drag coefficient	–
C_P, C_T	Power and thrust coefficients	–
C_x, C_y, C_z	Thrust coefficient components	–
f_e	Equivalent flat plate area	m^2
f_G	Ground effect factor	–
g	Gravitational acceleration	$\mathrm{m\,s}^{-2}$
h	Height above ground/sea level	m
H_R	Height of rotor hub	m
K_{ind}	Induced power factor	–
L	Longest Common SubSequence	–
m	Mass	kg
R	Main rotor radius	m
S	Similarity measure	–
$\underline{u}$	Control variable vector	
$\overline{U}_c$	Normalized velocity $\perp$ to TPP	–
$\overline{U}_t$	Normalized velocity $\parallel$ to TPP	–
u, v, w	Ground velocity components	$\mathrm{m\,s}^{-1}$
u_w, v_w, w_w	Wind velocity components	$\mathrm{m\,s}^{-1}$
v_{hov}	Induced velocity in hover	$\mathrm{m\,s}^{-1}$
$\overline{v}_i$	Normalized induced velocity	–
V	Speed	$\mathrm{m\,s}^{-1}$
$\underline{x}$	State variable vector	
x, y, z	Position coordinates	m
μ	Bank angle rad	
$\tilde{\mu}$	Advance ratio	–
ρ	Air density	$\mathrm{kg\,m}^{-3}$
σ	Rotor solidity	–
τ	Normalized time	–
ϕ	Azimuth angle	rad
χ	Heading angle	rad
Ω	Main rotor rotation speed	$\mathrm{rad\,s}^{-1}$

Presented at the Vertical Flight Society's 81st Annual Forum & Technology Display, Virginia Beach, VA, USA, May 20–22, 2025.

INTRODUCTION

The Royal Netherlands Navy (RNLN) leverages the capabilities of maritime helicopters to enhance its operational effectiveness. Maritime helicopters are flexible multirole vehicles, capable of performing a wide range of operations, and are essential in combination with small-deck ships. Maritime aerial vehicles regularly operate in challenging environments, due to the interaction with the moving ship, the wind, and the sea state, which can lead to highly dangerous situations. The most demanding flight phase is the recovery maneuver, involving the safe approach and landing of the helicopter on the ship deck. For crewed operations, the ship is in full service of

the helicopter, meaning that the vessel is obliged to maneuver to obtain optimal wind conditions for the helicopter. This is not desirable when operating with multiple Unmanned Aerial Vehicles (UAVs), as they should be able to take off and land frequently, and in relatively higher numbers.

Operational flight envelopes are established to reduce the safety risks of maritime recovery operations. They represent the combination of wind speed and relative direction to the ship for which the helicopter can safely approach and land on the ship deck. The boundaries of the safe envelopes are known as Ship-Helicopter Operating Limits (SHOLs) for manned aircraft, or Ship-UAV Operating Limits (SUOLs) for unmanned aircraft. The approach phase is typically constrained by relative wind direction and speed, whereas the landing phase is mostly bounded by deck motions such as pitch, roll, and heave. Operating outside these boundaries is generally not permitted, except for extreme circumstances (Ref. 1).

Determining the SHOLs is a time-consuming and expensive task, and is established through multiple weeks of intensive flight trials (Ref. 2). These flight trials might become dangerous for pilots since helicopter limits are approached for various weather conditions. Therefore, research has been conducted to create simulation environments in which SHOLs can be estimated from helicopter and/or pilot prediction models (Refs. 3–8).

Because wind greatly affects ship-helicopter operations, several studies have evaluated the effects of wind on shipboard-helicopter operations, and developed CFD models that accurately describe turbulence (Ref. 9). Some studies have used wind tunnel tests to investigate the effects of helicopters on ships (Ref. 10), while others have examined flow properties obtained from CFD simulations together with actual flight tests (Ref. 11). Relative winds from the starboard and port sides have been found to have different effects due to the asymmetry of the ship, which should be taken into account when determining operational limits (Ref. 12). Winds also lead to higher control efforts and modified ground effect behavior above the flight deck.

In the last decade, UAVs have soared in the supply-and-demand chain and have been proven to be superior to manned helicopters for certain operations. This is especially because they are cheaper, expendable, require less fuel, and can be deployed much more frequently than crewed vehicles. Because of these advantages, the RNLN wishes to deploy UAVs from Navy ships. At the same time, this new field of applications has opened new research lines, including ship-UAV recovery operations (Refs. 13–16). On this topic, the Netherlands Defense Academy (NLDA) has collaborated with the Netherlands Aerospace Center (NLR) and Maritime Research Institute Netherlands (MARIN) within the NOTUS project. This project aimed to create a simulation environment in which UAVs can land autonomously on moving ship decks, in order to determine SHOLs in adverse weather situations systematically. Among the other outcomes, the project produced a flight controller capable of landing the UAV by predicting future ship deck motions (Ref. 17). More recently, the NLDA, NLR, and German Aerospace Center (DLR) launched the SpeedOps (ShiP-deck Environment and Efficient Drone Operations) project, which aims to evaluate wind conditions around the ship deck to automate drone launch and recovery operations (Ref. 18).

Operational envelopes and their limits are tied to standardized approach maneuvers (Refs. 19, 20), which are not yet defined for unmanned systems. This justifies investigating optimal approach trajectories that are free from *operational* constraints, and for the cases in which the ship does not have to maneuver to accommodate for the UAV. SUOLs can then be determined from the optimal paths in the extreme cases where *performance* constraints are not met.

Previous studies on unmanned rotorcraft developed flight controllers to counteract wind disturbances (Refs. 12, 21), optimized obstacle-avoidance performance, or optimized performance in wind-free paths and investigated the effects of wind on the vehicle on this pre-determined path (Ref. 22). A substantial body of research focused on optimizing trajectories for minimum noise footprint and emissions, using helicopter models with 3 or 6 Degrees of Freedom (DoF) and occasionally including uniform wind conditions (Refs. 23–27). One study proved that optimal path-performance may lead to different approach and landing trajectories than conventional ones (Ref. 28). However, no systematic research has been conducted on optimal helicopter-ship approach trajectories in a windy atmosphere.

The main objective of this research is to assess the impact of wind direction, speed, and profile on optimal UAV-ship approaches. To fulfill this objective, optimal approach trajectories are obtained using a global path-performance optimization framework based on Optimal Control Theory. This framework combines the simulation of rotary-wing UAV dynamics in a certain wind field with the prescribed motion of a sailing vessel. Analyzing the resulting flight trajectories on the basis of performance constraints allows providing new operational guidelines without the need for actual flight tests. For example, high wind intensity for a given wind direction may prevent the existence of any optimal approach trajectory in light of the given UAV performance characteristics, such as the power available from the engine. In such cases, operational limits can be identified.

The optimal approaches of the studied UAV are assumed to also comply with comparable aircraft, allowing newly purchased UAVs to be deployed quickly. Furthermore, the optimal approach maneuvers from this study can aid as guidelines for new UAV approach maneuvers, supporting future research activities, and maritime UAV operations conducted by the RNLN or Coastguard.

Figure 1 presents a high-level overview of the models concurring into optimization framework. Each of these models is described in more detail in the following sections.

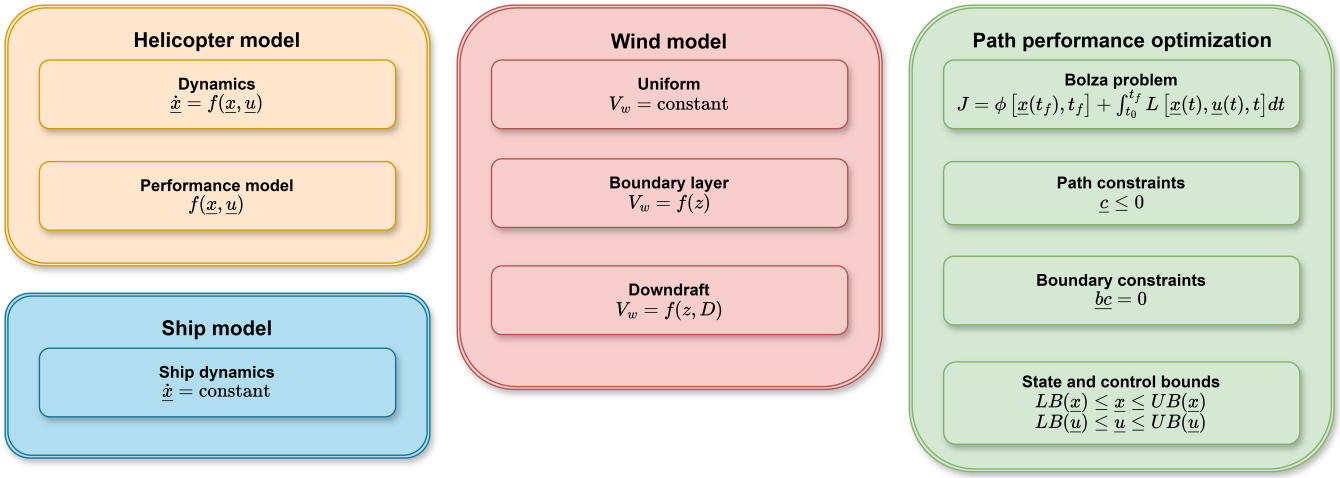

Figure 1: High-level overview of the developed simulation model

VEHICLE MODELS

Helicopter dynamics

The helicopter is modelled as a point-mass with 3 translational DoF, whose motion is commanded by three independent thrust coefficients. These variables embed the actual control inputs in terms of collective, cyclic and pedal, avoiding the need to model the system at such low-level of detail. Cross-coupling dynamic effects are neglected to decrease model complexity, improve optimization convergence rate, and reduce computational time. The equations of motion are written in terms of ground speed and position in a fixed Earth reference frame, therefore including the effect of wind on aerodynamic drag and body accelerations. The system of equations of motion is closed by three kinematic equations (Ref. 25) and the International Standard Atmosphere (ISA) model with $g = 9.80665\,\mathrm{m\,s^{-2}}$, as reported in the following Equation (1).

$$\begin{aligned}
\dot{u} &= \frac{1}{m}\left(C_x \rho (\Omega R)^2 \pi R^2 - f_e \frac{1}{2}\rho (u - u_w) V_{\mathrm{TAS}}\right) \\
\dot{v} &= \frac{1}{m}\left(C_y \rho (\Omega R)^2 \pi R^2 - f_e \frac{1}{2}\rho (v - v_w) V_{\mathrm{TAS}}\right) \\
\dot{w} &= \frac{1}{m}\left(C_z \rho (\Omega R)^2 \pi R^2 - f_e \frac{1}{2}\rho (w - w_w) V_{\mathrm{TAS}} - mg\right) \\
\dot{x} &= u \\
\dot{y} &= v \\
\dot{z} &= \dot{h} = w
\end{aligned} \tag{1}$$

The True Airspeed (TAS) is calculated as:

$$V_{\mathrm{TAS}} = \sqrt{(u - u_w)^2 + (v - v_w)^2 + (w - w_w)^2} \tag{2}$$

Helicopter performance

The helicopter's performance model complements the set of equations of motion, and creates the possibility to impose physics-based performance constraints. The engine power coefficient is computed as in the following Equation (3) (Refs. 25, 26, 29).

$$C_{P_{\mathrm{req}}} = C_T \sqrt{\frac{C_W}{2}}\left(K_{\mathrm{ind}} f_G \bar{v}_i + \overline{U}_c\right) + \frac{1}{8}\sigma c_d \left(1 + 4.65\tilde{\mu}^2\right) \tag{3}$$

Here, the $K_{\mathrm{ind}} = 1.15$ coefficient takes non-uniform flow into account and c_d is the mean profile drag coefficient. The thrust coefficient is calculated as in Equation (4).

$$C_T = \sqrt{C_x^2 + C_y^2 + C_z^2} \tag{4}$$

The weight is calculated as in Equation (5), and related to the induced velocity in hover v_{hov}.

$$C_W = \frac{W}{\rho(\Omega R)^2 \pi R^2} = 2\left(\frac{v_{\mathrm{hov}}}{\Omega R}\right)^2 = 2\bar{v}_{\mathrm{hov}}^2 \tag{5}$$

The normalized velocities perpendicular and tangential to the TPP ($\overline{U}_c$ and $\overline{U}_t$, respectively) are computed as shown in Equations (6) and (7) (Ref. 25). $\overline{U}_c$ is also called the normalized main rotor climb velocity.

$$\overline{U}_c = \frac{uC_x + vC_y + wC_z}{v_{\mathrm{hov}} C_T} \tag{6}$$

$$\overline{U}_t = \frac{\left[\begin{array}{r} u^2(C_y^2 + C_z^2) + v^2(C_x^2 + C_z^2) + w^2(C_x^2 + C_y^2) + \\ -2uvC_xC_y - 2uwC_xC_z - 2vwC_yC_z \end{array}\right]^{\frac{1}{2}}}{v_{\mathrm{hov}} C_T} \tag{7}$$

The normalized induced velocity through the main rotor is calculated as in Equation (8), depending on whether the helicopter is inside or outside the vortex ring state (Refs. 23, 24).

$$\bar{v}_i = \begin{cases} \arg\left\{\bar{v}_i^4 + 2\overline{U}_c\bar{v}_i^3 + (\overline{U}_c^2 + \overline{U}_t^2)\bar{v}_i^2 = 1\right\} & \text{if inside} \\ \overline{U}_c(0.373\overline{U}_c + 0.598\overline{U}_t - 1.991) & \text{otherwise} \end{cases} \tag{8}$$

The normalized induced velocity outside the vortex ring state must be solved iteratively, while the one inside the vortex ring

state can be computed directly. The helicopter is inside the vortex ring state if the inequality in the following Equation (9) is verified.

$$(2\overline{U}_c + 3)^2 + \overline{U}_t^2 > 1 \tag{9}$$

Operating in this condition is considered dangerous and should be avoided.

The ground effect has a major impact on the lift performance of the main rotor, reducing the power required to fly or hover. Because the helicopter approaches the ship in this study, the aircraft flies close to the deck at some point in time and thus will be affected by the ground effect. It is modelled by point-mass equations combined with a source model (Refs. 23, 30). Note that the point-mass equations of motions describe the dynamics of the center of gravity, which is assumed to be located at the center of the rotor disk. On the other hand, the model for the ground effect takes into account the height of the rotor hub above the ground, as shown in Equation (10).

$$f_G = 1 - \frac{R^2 \cos^2 \theta_w}{16(h + H_R)^2} \tag{10}$$

In this relation, H_R is the height of the main rotor hub with respect to the ground, and θ_w is the angle between the rotor wake and a vertical reference line. The latter is calculated from the following Equation (11)

$$\frac{1}{\cos^2 \theta_w} = 1 + \frac{\left(C_T \sqrt{u^2 + v^2} + v \sqrt{C_x^2 + C_y^2}\right)^2}{wC_T + vC_z^2} \tag{11}$$

where

$$v = K_{\text{ind}} v_{\text{hov}} \bar{v}_i f_G \tag{12}$$

The ground effect equations need to be solved iteratively as well.

Equation (3) includes the induced power, power to climb and profile power, but neglects secondary effects such as tail rotor power and additional installation losses. While these components could consume around 15% of engine power, such approximation is accepted as a modelling safety margin is embedded in the specification of the power available. The dimensional power required is computed using the definition of Equation (13).

$$P_{\text{req}} = C_{P_{\text{req}}} \rho (\Omega R)^3 \pi R^2 \tag{13}$$

Reference helicopter

This study utilizes the PH-1AA Orange Eye helicopter, shown in Figure 2, as a test case. This small, unmanned conventional helicopter has a main rotor diameter of 3.3 m, an empty weight of 60 kg and maximum weight with payload of 100 kg. Furthermore, the maximum engine power is $P_a = 10.5$ kW, the maximum thrust coefficient is $C_{T_{\max}} = 0.0059$ and its cruise speed is equal to $V_{\text{cr}} = 27\,\text{m}\,\text{s}^{-1}$. A real model of this aircraft is owned by the Netherlands Aerospace Center (NLR). It was originally equipped with a gas turbine, but now the propulsion system is electric. This UAV is primarily used for experimental research and represents the future deployment of

Figure 2: PH-1AA Orange Eye helicopter

other UAVs by the RNLN. This helicopter is used in former projects and has provided insight into ship-UAV interactions and landings (Ref. 17).

Reference ship

Similar to the helicopter, the ship's deck is also modelled as a point-mass. In this study, the vessel sails North in a calm sea with constant velocity and heading, without being affected by effects such as sea state or wind. Deck motions are excluded as only the approach is studied in this project. The model incorporates the ship's dimensions for collision avoidance, effectively treating the vessel geometry during the trajectory optimization problem. The total ship model is given in Equation (14), where the chosen values of the velocity is suitable for a patrol vessel during standard operations in calm sea conditions.

$$\begin{aligned} \dot{u}_{\text{ship}} &= 0 \qquad & \dot{x}_{\text{ship}} &= u_{\text{ship}} = 16\,\text{kts} \\ \dot{v}_{\text{ship}} &= 0 \qquad & \dot{y}_{\text{ship}} &= v_{\text{ship}} = 0\,\text{kts} \\ \dot{w}_{\text{ship}} &= 0 \qquad & \dot{z}_{\text{ship}} &= w_{\text{ship}} = 0\,\text{kts} \end{aligned} \tag{14}$$

A Holland-Class Ocean-Going Patrol Vessel (OPV) acts as the UAV's mothership, as depicted in Figure 3. Four patrol vessels of this type, with a length of 108 m and width 16 m, have been actively serving in the RNLN since 2012, and are primarily deployed in low-violence areas, such as counter-drugs operations near the Caribbean coasts. The length of the helicopter deck is 28 m.

WIND MODELS

Three wind models are utilized in this study, and are compared to the baseline no-wind condition: a uniform wind field, an Atmospheric Boundary Layer (ABL) wind field, and a model to locally describe the downdraft near the helicopter deck.

Uniform wind field

For this first model, the wind velocity is assumed parallel to the ground, and constant in module and direction at every position and altitude in the domain. Two horizontal wind speed

Figure 3: Holland-Class Ocean-Going Patrol Vessel of the RNLN

components are sufficient to characterize this wind field depending on the assigned wind speed V_w and direction, defined in terms of the azimuth angle ϕ_w. The wind speed components in the Earth Reference frame are calculated as in Equation (15).

$$u_w = V_w \cos\phi_w \qquad v_w = -V_w \sin\phi_w \qquad w_w = 0 \tag{15}$$

Atmospheric Boundary Layer (ABL) wind field

Due to surface roughness and viscous friction, wind speeds tend decrease when nearing the Earth surface, introducing shear layers which depend on altitude. The shape of such ABL depends on several atmospheric parameters (Refs. 31, 32), but is commonly modeled using the power law of Equation (16).

$$\frac{V_w}{V_{\text{ref}}} = \left(\frac{z}{z_{\text{ref}}}\right)^{\alpha} \tag{16}$$

The power law computes the wind speed V_w as a function of altitude z when the velocity V_{ref} is known at a reference height z_{ref}. This reference velocity can be found from real-time measurements from buoys[A] or from the ship's own wind measurement system. The value of the α exponent dictates the shape of the velocity curve, and depends on surface roughness and atmospheric stability (cityscape, forest canopy, flat sea). This equation is frequently used in engineering for its simplicity and ability to provide accurate results, which in this case have been validated by more advanced models (Ref. 33).

For the present applications, the reference wind speed varies in a systematic sensitivity study. The reference altitude is fixed at $z_{\text{ref}} = 20\,\text{m}$. The value of the exponent is fixed at $\alpha = 0.11$, which is applicable for a wind profile under near-neutral stability conditions at sea (Ref. 34). The conversion from wind speed and azimuth angle to wind components in the Earth axes system is carried out again as in Equation (15). The resulting wind profile is shown in Figure 4.

[A]National Oceanic and Atmospheric Administration (NOAA). National Data Buoy Center. NASA - Langley Research Center - Turbulence Modeling Resource. URL: https://www.ndbc.noaa.gov. Accessed: April 25, 2025

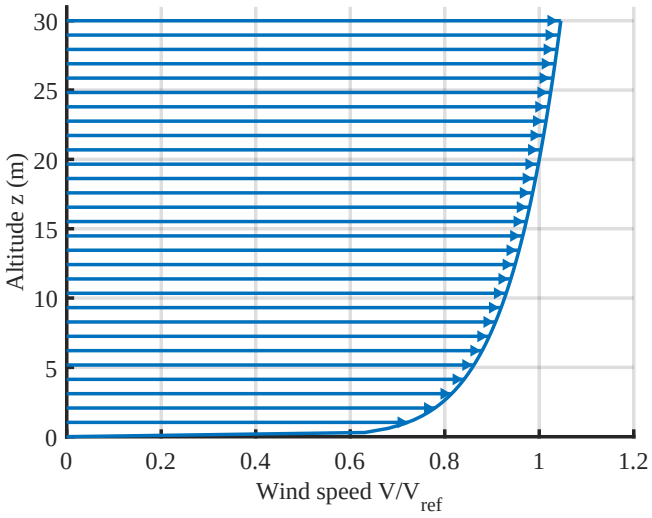

Figure 4: Atmospheric Boundary Layer wind profile

Downdraft behind the hangar

On top of macroscopic, free-stream wind fields, a more detailed model around the helicopter deck can be employed to influence the helicopter performance near the landing spot. Free-stream airflow interacts with a bluff body such as a ship's superstructure, resulting in a circulation zone behind the body. This means that helicopters typically experience a downdraft near the landing spot, effectively increasing their power required to fly. Next to this, airflow velocity behind the body tends to decrease, resulting in the phenomenon of "velocity deficit", which also affects the helicopter's performance (Ref. 11).

A simple downdraft model is developed to enrich the ABL model with such local effects. The model is developed on the basis of an experimental dataset resulting from wind tunnel experiments on airflow around high-rise buildings (Ref. 35). It utilizes the relative airflow perceived at the hangar roof height above the sea, as calculated by the ABL model. It results in the airflow pattern as illustrated in Figure 5.

Simulations performed with such downdraft model include two downdraft strengths (10% and 20% of the relative free stream flow), with and without the velocity deficit of 20%, which are in line with previous research (Ref. 11). In this way, both effects are isolated and enables independent analysis. The velocity deficit is only applied to the horizontal component of the true wind speed.

PATH PERFORMANCE OPTIMIZATION

Path performance optimization employs dynamic simulation to optimize a given flight metric over the entirety of the approach path, while complying with assigned performance and geometric constraints. In the scope of this research, this is achieved by finding appropriate time histories of the input variables that are used to propagate the dynamics of the system. Because input variables are also called "control variables", the path performance optimization problem is also referred to as an Optimal Control Problem (OCP) (Refs. 36,37).

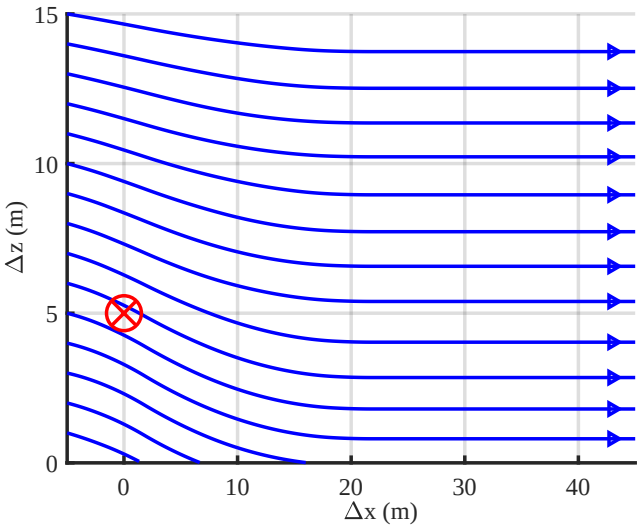

Figure 5: Streamlines of airflow at the helicopter deck, including downwash, in the downdraft wind model. The red marker indicates the final helicopter position before the landing maneuver.

States and control variables

From a quick inspection of Equation (1), the most intuitive choice for the control variables falls on the thrust coefficient components C_x, C_y and C_z. However, control inputs can typically exhibit fast-varying time histories, dictated by an aggressive behavior of the OCP solver, which tends to converge towards bang-bang-type of solutions. This behavior is not really realistic, negatively impacts the convergence, and requires a significantly larger amount of iterations (Ref. 27). Therefore, artificial control variables are defined as the rate of change of the thrust coefficient components, as defined in Equation (17).

$$\underline{u} = [u_1, u_2, u_3]^T = \left[\dot{C}_x, \dot{C}_y, \dot{C}_z\right]^T \tag{17}$$

This has the effect to smoothen the trajectory, increase convergence, damp control efforts and partially simulate actuator response delays (Ref. 24). No constraints are imposed on these pseudo-controls.

This "control damping" artifice upgrades the thrust coefficients C_x, C_y and C_z to states, reaching a total of 9 state variables for the helicopter, as shown in Equation (18).

$$\underline{x} = \left[u, v, w, x, y, z, C_x, C_y, C_z\right]^T \tag{18}$$

This requires adding the following three trivial differential equations to the ones reported in Equation (1).

$$\dot{C}_x = u_1 \qquad \dot{C}_y = u_2 \qquad \dot{C}_z = u_3 \tag{19}$$

In light of this, state constraints can now be imposed directly on the thrust coefficients, removing the necessity to define complex non-linear constraints on the thrust value, and therefore lowering the overall computational cost of the OCP.

Since the ship velocities are fixed, its positions change linearly in time and are not affected by the helicopter control variables. Therefore, the ship's dynamic evolution is perfectly predictable, and can be computed directly. It effectively acts as a time-dependent constraint for the helicopter evolution.

Scaling has been applied to ensure that the state, control and independent variables are of similar magnitudes, in order to improve the convergence of the optimization algorithm (Refs. 23, 25). The augmented state and control variables that are actually used during the numerical solution of the OCP are reported in the following Equation (20).

$$\begin{gathered} x_1 = \frac{10u}{\Omega R} \qquad x_2 = \frac{10v}{\Omega R} \qquad x_3 = \frac{10w}{\Omega R} \\ x_4 = \frac{x}{10R} \qquad x_5 = \frac{y}{10R} \qquad x_6 = \frac{z}{10R} \\ u_1 = 10^3 \frac{\mathrm{d}C_x}{\mathrm{d}\tau} \qquad u_2 = 10^3 \frac{\mathrm{d}C_y}{\mathrm{d}\tau} \qquad u_3 = 10^3 \frac{\mathrm{d}C_z}{\mathrm{d}\tau} \\ \tau = \frac{t\Omega}{100} \end{gathered} \tag{20}$$

Objective function

The objective is to get the helicopter on board the ship as smoothly and quickly as possible, for the given wind conditions, performance and geometric constraints. A smooth trajectory is characterized by a continuous flight path with little control actions. Therefore, a quadratic control penalty makes the Lagrange term of the objective function to avoid jittering of the control inputs. The value of the final time instant makes the end-cost or Mayer term of the objective function. A weighting factor K_{t_f} is added to match the magnitudes of both contributions and tune the importance of time compared to the control effort. The expression of the objective function is shown in Equation (21), in terms of non-dimensional variables.

$$J = K_{t_f} \tau_f + \int_{\tau_0}^{\tau_f} \left(u_1^2 + u_2^2 + u_3^2\right) d\tau \tag{21}$$

From a preliminary sensitivity analysis, a value of $K_{t_f} = 10^{-3}$ was chosen, balancing control smoothness and mission duration.

Constraints

Helicopter performance constraints must be satisfied along the entire path to achieve a feasible result. All imposed performance constraints are summarized in Table 1. Most constraints can be imposed directly. However, two require extra attention and are described below.

Firstly, the maximum bank angle is restricted to prevent the helicopter from making overly steep turns and from flying upside down. Its value is calculated, as in Equation (22), assuming a steady turn, where $\dot{\chi}$ is the rate of change of the heading angle.

$$\tan\mu = \frac{\dot{\chi} V}{g} \quad \text{with} \quad \dot{\chi} = \frac{u\dot{v} - \dot{u}v}{u^2 + v^2} \tag{22}$$

Table 1: Path constraints

Type	Expression
Max. thrust coefficient	$C_T \leq C_{T_{\max}} \rho_0/\rho(z)$
Rotor upward thrust	$C_z \geq 0$
Power available	$P_{\text{av}} \geq P_{\text{req}}$
Max. bank angle	$\mu \leq \mu_{\max}$
Collision avoidance	$C \geq 0$
Min. Safe Altitude (MSA)	$h > h_{\min}$
Never Exceed speed	$V_{\text{TAS}} \leq V_{\text{NE}}$

Its maximum value is set to $\mu_{\max} = 30°$, in accordance with the prescription of the Aeronautical Design Standard 33 (ADS-33) for aggressive agility in forward flight (Ref. 38). Aggressive agility is justified since the studied vehicle is unmanned, making passenger comfort irrelevant. Additionally, this maximum bank angle results in a maximum load factor of about 1.15 in a medium turn, which does not have detrimental effects on flying qualities (Ref. 39). In any case, the helicopter remains free to turn tightly by adjusting its flight speed (Ref. 26).

Secondly, it is essential to avoid collisions between the helicopter and ship. To do so, the ship is regarded as a moving parallelepiped, and two "NoGo Zones" are defined with respect to its dimensions as shown in Figure 6. The Hard NoGo Zone identifies the ship minus the flight deck, while the Safe NoGo Zone is the Hard zone enlarged with a clearance equal to the helicopter's main rotor diameter (Ref. 40).

If the position of the faces of a NoGo Zone are denoted as $X_1(t)$, $X_2(t)$, $Y_1(t)$, $Y_2(t)$, $Z_1(t)$, and $Z_2(t)$, the condition for the helicopter's position to lie outside the NoGo Zone is given by Equation (23)

$$C = 2|\mathbb{X}||\mathbb{Y}||\mathbb{Z}| + \mathbb{X}|\mathbb{Y}||\mathbb{Z}| + |\mathbb{X}|\mathbb{Y}|\mathbb{Z}| + |\mathbb{X}||\mathbb{Y}|\mathbb{Z} \geq 0 \quad (23)$$

where

$$\mathbb{X} = \frac{(x-X_1)(x-X_2)}{X_2(t)-X_1(t)} \qquad \mathbb{Y} = \frac{(y-Y_1)(y-Y_2)}{Y_2(t)-Y_1(t)}$$
$$\mathbb{Z} = \frac{(z-Z_1)(z-Z_2)}{Z_2(t)-Z_1(t)} \quad (24)$$

In other words, collision occurs when $C < 0$, meaning that $\mathbb{X} < 0$, $\mathbb{Y} < 0$ and $\mathbb{Z} < 0$.

Additionally, to restrict the helicopter's descent below the landing height, a Minimum Safe Altitude (MSA) of $h_{min} = 5\text{m}$ is defined.

Lastly, the maximum helicopter speed is bounded by condition of reversed flow on the retreating blade, as it can be expected for helicopters with a small tip speed ΩR. The Never Exceed Speed V_{NE} is reached for an advance ratio of $\tilde{\mu} = 0.4$ (Ref. 41), and is equal to $V_{\text{NE}} = 52.3\,\text{m}\,\text{s}^{-1}$.

Boundary conditions

The simulation starts with the helicopter and ship in assigned positions. At the initial condition, the helicopter is demanded to fly horizontally at cruise speed, with no accelerations. The optimizer is free to adjust for the initial heading in each scenario.

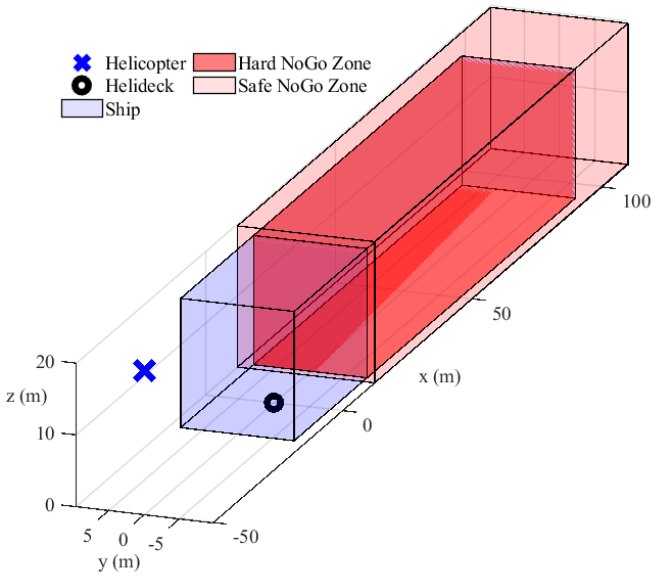

Figure 6: NoGo Zones utilized for the collision-avoidance path constraint, with feasible helicopter position ($C \geq 0$), to scale.

Table 2: Boundary conditions

Type	Expression
Initial position	$x = x_0$, $y = y_0$, $z = z_0$
Initial speed	$V = V_{\text{cr}}$, $w = 0$
Initial acceler.	$\dot{u} = \dot{v} = \dot{w} = 0$
Final position	$x = x_{\text{ship}}(t_f)$, $y = y_{\text{ship}}(t_f)$, $z = z_f$
Final velocity	$u = u_{\text{ship}}$, $v = v_{\text{ship}}$, $w = 0$
Final acceler.	$\dot{u} = \dot{v} = \dot{w} = 0$

At the final condition, the helicopter is demanded to be in a steady hover above the flight deck relative to the moving ship, meaning that its ground velocity equals the ship's ground speed and all accelerations are zero. This configuration reflects the vehicle being positioned above the flight deck, preparing to land. Because the ship moves throughout the maneuver, the UAV's final position must be defined relative to the ship's final location. Thus, the final boundary condition on position is time-dependent and is updated using the ship's motion model.

The imposed boundary conditions are summarized in Table 2.

Solver

The OCP is transcribed into a Nonlinear Programming (NLP) problem using the direct collocation method as implemented in the ICLOCS2 software framework (Ref. 42). The algorithm is widely used and validated for many OCPs, including multi-phase problems, and supports automatic mesh refinement. The Hermite-Simpson discretization method is used to

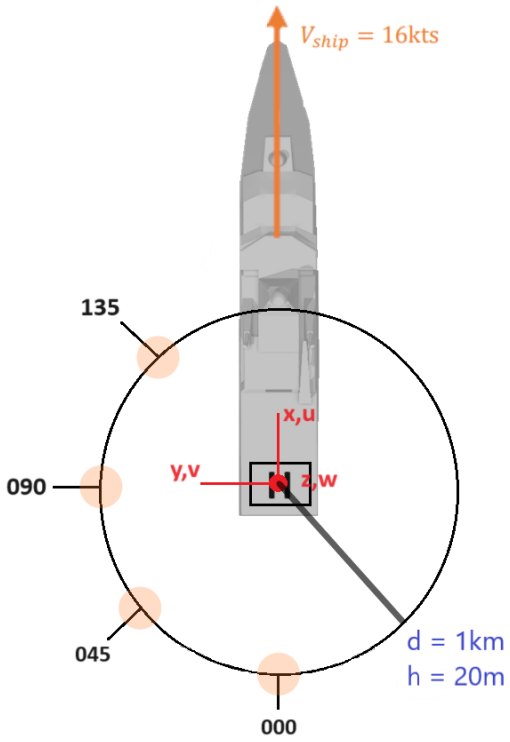

Figure 7: Initial conditions for all experiments

reconstruct the time histories of control variables using piece-wise quadratic polynomials, and the ones of state variables using piece-wise cubic polynomials (Ref. 43).

The resulting NLP problem is solved using the Sequential Quadratic Programming (SQP) algorithm implemented in the MATLAB `fmincon` function[B]. This method was selected after a preliminary exploration phase for being computationally faster (despite requiring more iterations (Ref. 44)), exhibiting good computational stability near vortex-ring and ground-effect conditions, being tunable and transparent during the optimization steps, and overall resulting in more robust optimization runs across the different wind models and starting positions.

EXPERIMENT MATRIX

All experiments follow a similar setup, which can be explained with the aid of Figure 7.

The helicopter starts at a distance of 1 km from the ship, in relative angles ϕ_0 of values 000°, 045°, 090° and 135°, meaning that the helicopter views the landing spot in these azimuth angles. The position in front of the ship ($\phi_0 = 180°$) is excluded, as an approach from this location is considered impractical and not operationally feasible. Wind blows towards all directions ϕ_w of the compass, in steps of 45°, with speeds varying from 0 kts to 40 kts in steps of 10 kts. A wind speed of 40 kts is equivalent to wind force 8 on Beaufort's scale. The ship sails in calm waters at a constant speed of 16 kts to the North without any heading changes. The approach ends when the helicopter is in a steady hover relative to the vessel, 5 m above the flight deck.

The matrix of experiments is analyzed, to different extents, for the three wind models presented earlier. Its extent is reduced by exploiting symmetry considerations in the following ways:

1. only initial helicopter positions in the left half-plane of the ship are considered;
2. in the case of the 000° starting position, results of the simulations for winds coming from the right half plane (to directions 225° to 315°) are mirrored for the symmetric wind direction.

The downdraft wind model is analyzed only for Northerly and Southerly winds, for which the downdraft is expected to be strongest. The outcomes are assumed to be similar for every initial helicopter location, so only the initial 000° position is studied. Two downdraft strengths (10% and 20% of local flow speed) and a 20% horizontal velocity deficit are applied.

Table 3 shows the simulations conducted for each wind model, with their intended purposes.

SIMILARITY ANALYSIS

A similarity analysis is conducted to quantify the difference between each optimal approach trajectory (for a given initial position, wind intensity and wind direction) and the corresponding wind-free scenario. Two geometrically similar trajectories typically share similar time histories (required power, thrust coefficient), while different paths often show deviations in performance parameters. This is due to increased engine demand or active performance constraints. A deviation from the reference does not imply that the approach is impractical, only that the wind makes it significantly different, and therefore worthy of attention for operational reasons. This comparative assessment provides a synthetic representation of the influence of different wind conditions on optimal approach paths.

The Longest Common SubSequence (LCSS) has been chosen to quantify the similarity between two trajectories (Ref. 45). The LCSS method is frequently utilized for noisy signal data and time series with different lengths or time steps, as the procedure is robust, can handle outliers and unmatched data points, and is less computationally expensive than other similarity techniques (Ref. 46). Additionally, it also allows normalizing the output to fall between 0 (no similarity) and 1 (perfect resemblance), which provides a uniform and intuitive way to interpret the results across the different scenarios.

Although many extensions of this procedure exist, including derivatives or optimization schemes (Refs. 46, 47), the standard Bottom-Up Matrix formulation[C] is implemented in this study and shortly described as follows. The two trajectories to be compared are indicated as the A and B sequences in Equation (25). They consist, in general, of a different number (n

[B] Matlab Optimization Toolbox. URL: https://nl.mathworks.com/products/optimization.html. Accessed: April 25, 2025

[C] Longest Common Subsequence (LCS). URL: https://www.geeksforgeeks.org/longest-common-subsequence. Accessed: April 25, 2025

Table 3: Matrix of simulated experiments

Wind model	**Initial position ϕ_0**	**Wind direction ϕ_w**	**Wind speed V_w**	**Analysis**
Uniform	000° to 135°	000° to 315°	0 kts to 40 kts	Effect of wind direction and speed
ABL	000° to 135°	000° to 315°	0 kts to 40 kts	Effect of wind shear
ABL + Downdraft	000°	000° 180°	0 kts to 30 kts 10 kts	Effect of local airflow

and m) of time stamps (t_i and t_j), each of which is associated to a three-dimensional position in space (a_i and b_j).

$$\begin{aligned} A &= \left[(t_1, a_1), ..., (t_n, a_n)\right] \\ B &= \left[(t_1, b_1), ..., (t_m, b_m)\right] \end{aligned} \tag{25}$$

For any two points a_i and b_j on the two trajectories, the infinity norm distance D_∞ between the two points is defined as in Equation (26) (Ref. 45).

$$D_\infty(a_i, b_j) = \max\left\{\left|a_{ix} - b_{jx}\right|, \left|a_{iy} - b_{jy}\right|, \left|a_{iz} - b_{jz}\right|\right\} \tag{26}$$

The LCSS $L_{i,j}$ between the two trajectories is then computed using a matrix of size $(n+1) \times (m+1)$, where the first row and column are initialized with zeros. The matrix is then filled recursively in a bottom-up manner by comparing the elements of the two sequences on the basis of the D_∞ norm, according to Equation (27).

$$L_{i,j} = \begin{cases} 0 & \text{if } i = 0 \text{ or } j = 0 \\ 1 + L_{i-1,j-1} & \text{if } D_\infty(a_i, b_j) \leq \varepsilon, |i - j| \leq \delta \\ \max(L_{i-1,j}, L_{i,j-1}) & \text{otherwise} \end{cases} \tag{27}$$

The last entry in the matrix diagonal contains the total amount of matched points between the two trajectories, and is effectively the measure of the LCSS between trajectories A and B, $L(A,B)$.

The algorithm depends on two tuning parameters. The ε parameters defines the minimum bounding envelope, which is the maximum distance threshold to consider two points to be similar. The δ parameter defines how far away these points should be within the data set for them to be considered similar. Therefore, positions close in space at different timestamps are considered to be similar only if the corresponding time instants are also within range. If the algorithm can find points on both trajectories that comply with thresholds ε and δ, they are considered similar enough and their LCSS score is increased on the diagonal of the L matrix.

The threshold parameters ε and δ are essential for the procedure, and are application dependent. This means that there is no generic method to tune these parameters. For the present studies, a value of δ = 30 was chosen on the basis of considerations on the average length of the trajectories and the time step size. The infinity norm is calculated separately for the horizontal or vertical projections of the trajectories, and therefore different values of ε are chosen accordingly. For the three-dimensional and horizontal paths $\varepsilon_{xyz} = \varepsilon_{xy} = 16\,\text{m}$ (equal to the ship's width), and for the vertical path $\varepsilon_z = 3.3\,\text{m}$ (equal to the helicopter's main rotor diameter).

The similarity function $S(A,B)$ based on the LCSS between trajectories A and B is defined as in Equation (28), and outputs a value in the interval $[0,1]$.

$$S(A,B) = \frac{L(A,B)}{\min\{n,m\}} \tag{28}$$

RESULTS

No wind baseline

The baseline scenario includes all four helicopter starting positions in the case of still atmosphere. The corresponding optimal trajectories towards the moving ship are shown in Figure 8. These will be used as references to comparatively evaluate all following results in windy atmosphere. All four trajectories are operationally predictable, exhibit smooth descents, and converge to the final hover position above the flight deck. For example, the trajectory corresponding to the initial position $\phi_0 = 135°$ shows very clearly how the helicopter needs to curve around the ship before aligning with the final approach corridor.

Further path- and performance-related parameters are reported in Table 4 and Figure 9. In the absence of wind, the True-Airspeed V_{TAS} equals the ground speed. While the starting locations are equidistant from the ship's initial position, paths from behind the ship require more time to complete, as the ship continues to move forward throughout the approach. This effect is also observable in the flight speed V_{TAS}, flight path angle γ and rotor disc angle of attack α_D graphs. Due to a combination of relatively low average distance to the ship and high initial helicopter velocity, the $\phi_0 = 135°$ starting point results in a sharper maneuver, corresponding to a higher control effort and peak power demand. Interestingly, the power peak for this trajectory occurs before the final hover phase, while for all the others it occurs during low-speed descent. To conclude, the baseline no-wind scenario resulted in smooth trajectories which are intuitively explainable and executable for operational ship-UAV approaches.

Uniform wind

Figure 10 displays the LCSS similarity scores S of optimal trajectories in a uniform wind field, as compared to the baseline no-wind scenario for all four starting positions. Colored markers indicate levels of similar power consumption

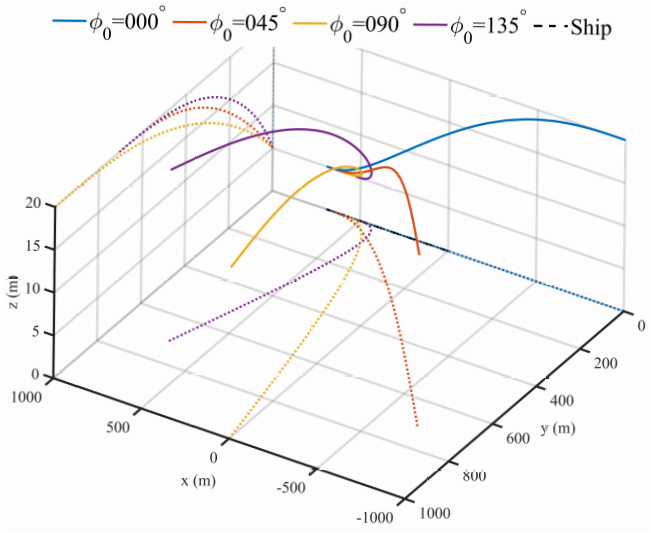

(a) Three-dimensional view with ground and North projections

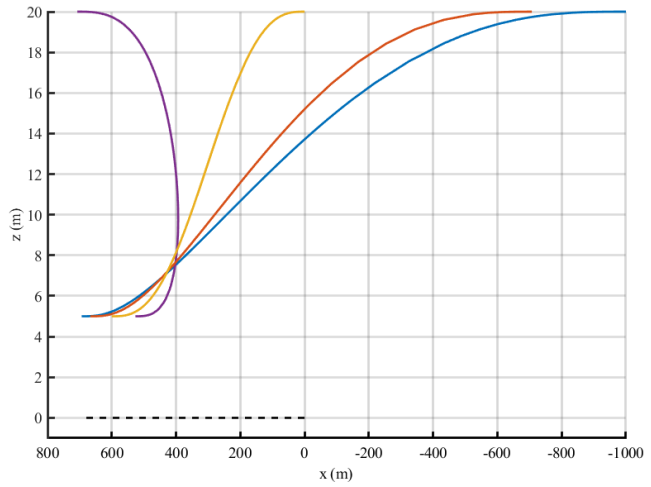

(b) View from West

Figure 8: Optimized helicopter trajectories for different initial positions in the baseline scenarios with no wind

(squares), active constraints (triangles) or non-converged solutions (circles). An active constraint (triangle) is to be considered within the solution tolerance bounds, meaning that the constraint is active in at least one point of the trajectory, but the trajectory is still feasible. A red circle indicates an infeasible path in the current numerical setup.

Initial positions $\phi_0 = 000°$ and $\phi_0 = 045°$ consistently reach the available power limit in the case of ship's headwinds. In these scenarios, the helicopter initially gains altitude to con-

Table 4: Flying time and distance covered for the baseline no-wind scenario

Initial pos. ϕ_0	**Flight time** t_f	**Flight distance**
000°	84.3 s	1693.8 m
045°	81.0 s	1545.5 m
090°	72.9 s	1166.4 m
135°	64.0 s	730.0 m

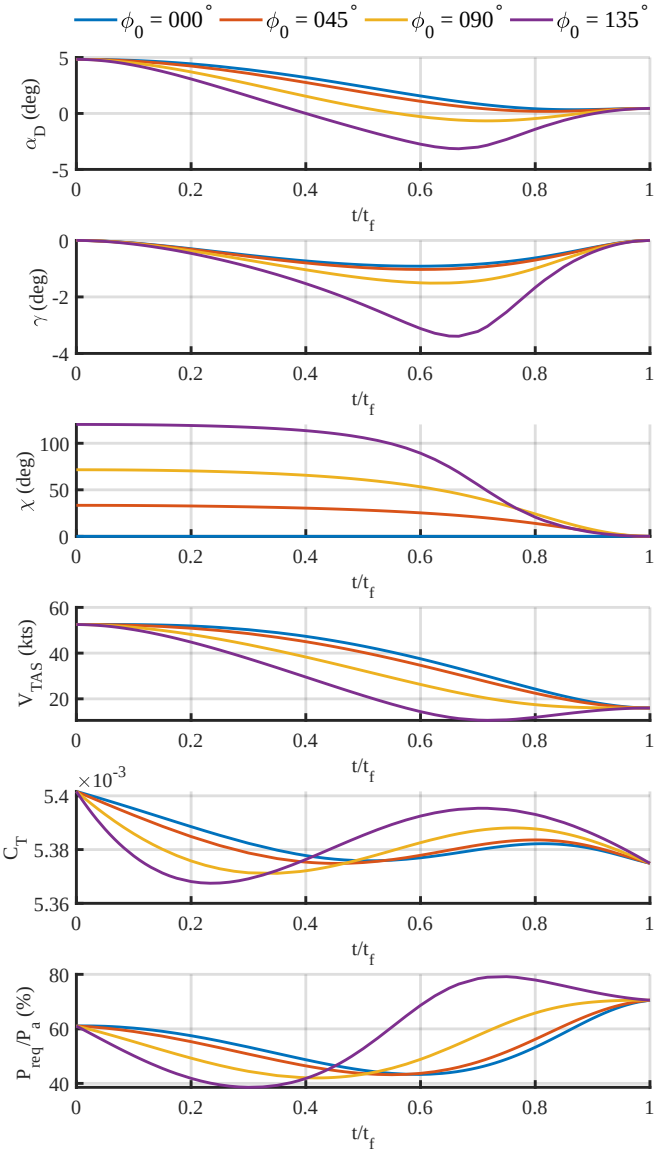

Figure 9: Trajectory and performance parameters for the baseline no-wind scenario

vert potential energy into kinetic energy in the final approach. The ship's headwind also increases power consumption for position $\phi_0 = 090°$, but not as much. Therefore, it seems to be more beneficial to approach the vessel from the side when dealing with strong Northerly winds.

The ship's crosswinds alter the baseline optimal paths so that the aircraft has to use the extra ground speed for positions $\phi_0 = 000°$ and $\phi_0 = 045°$, or was helped by decelerating in positions $\phi_0 = 090°$ and $\phi_0 = 135°$. Tailwinds, either during the approach or relative to the ship, can be problematic due to low airspeeds, increased power consumption and tail clearance with the flight deck. For positions $\phi_0 = 090°$ and $\phi_0 = 135°$, the NoGo Zone constraint was violated because the helicopter did not have enough distance to decelerate properly or enough power to complete the sharp maneuver. Due to this, location $\phi_0 = 135°$ suffered from several infeasible paths for winds from the North and North-West.

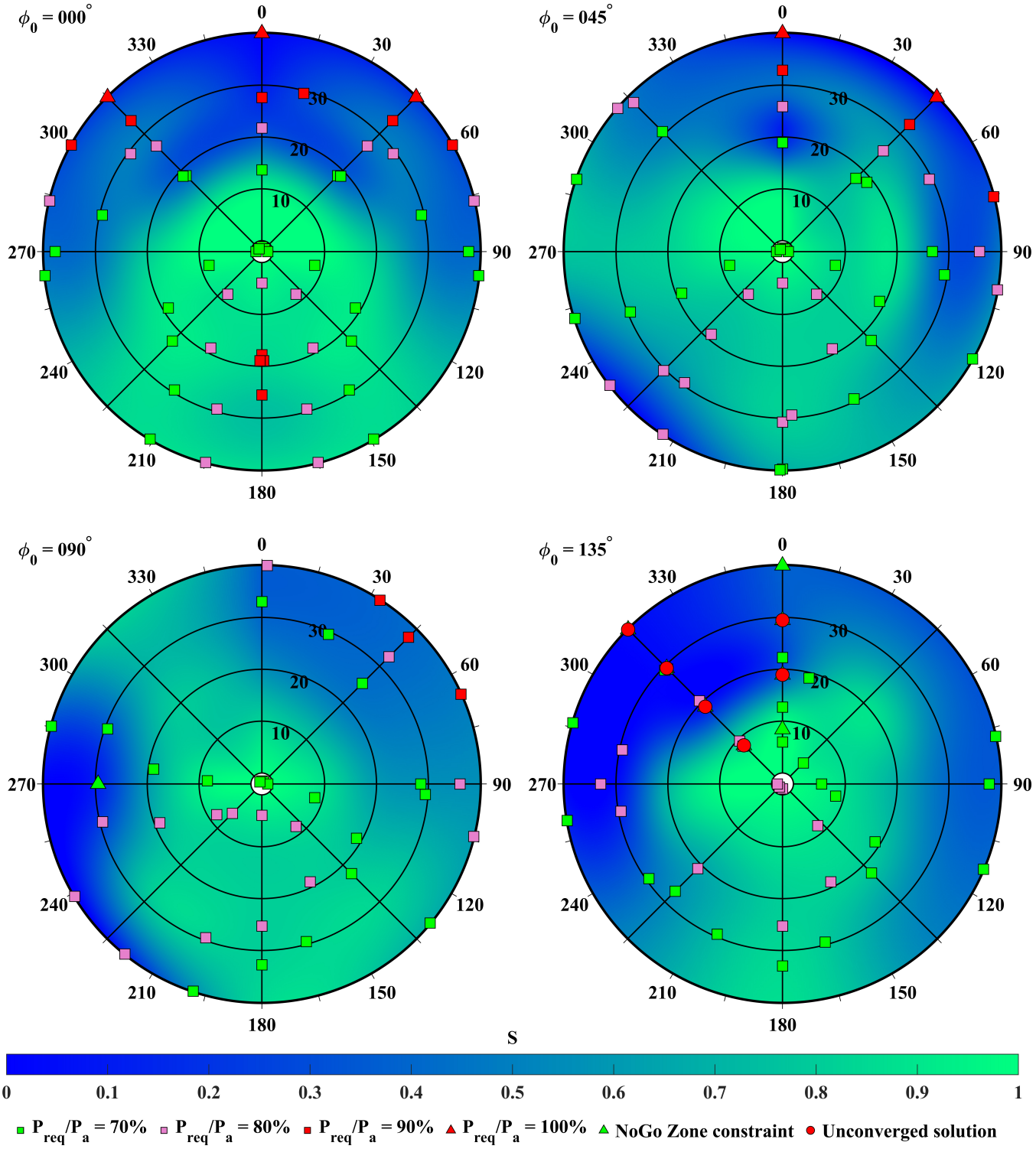

Figure 10: LCSS similarity measure S of optimal trajectories in uniform wind fields compared to the baseline no wind condition. A point in each plot corresponds to a different wind condition, with the azimuth angle indicating the wind direction and the distance from the center indicating the wind speed. Several markers indicate power consumption levels, active constraints and unconverged/infeasible solutions.

Figures 11a and 11b respectively show the helicopter starting position, for each wind condition, resulting in the minimum total objective function or in the minimum total energy consumption during the approach. The former is a combined measure of mission time with control effort, while the latter is calculated as the time-integral of the power required. Minimum-energy approaches are relevant for low-running batteries, One-Engine-Inoperative conditions, emergencies, or rough weather where landings require more power. In either case, this type of information is essential from an operational point of view. Paths that violate the NoGo Zone constraint are excluded from the comparison.

While some wind conditions result in the same best initial positions for both metrics, others differ. Fluctuations in the best initial positions seem to be mostly due to numerical deviations. In practical operations, it is advisable to maintain a consistent starting location for a given wind direction, even more so in light of the fact that wind speeds can be measured inaccurately due to sensor errors or local fluctuations. Thus, for operational purposes, it is best to start from position $\phi_0 = 135^\circ$ for Easterly winds, $\phi_0 = 000^\circ$ for winds from the South-East and South-West, and $\phi_0 = 090^\circ$ for Southerly winds in the case of a low objective function value, or either $\phi_0 = 000^\circ$ or $\phi_0 = 135^\circ$ for the lowest energy consumption. $\phi_0 = 090^\circ$ is best for Northerly winds.

Boundary layer wind

The same analysis presented in the previous section was repeated with the ABL wind field model, hence adding the effects of vertical wind shear. The results show a strong consistency with the uniform wind model in terms of similarity measures, constraints, and power demand trends. As expected, the ABL model introduces differences in the vertical behavior of the helicopter, showing that the UAV can exploit wind gradients to reduce its required power, mostly by flying at lower altitudes more often. However, NoGo Zone constraint violations remain similar to the uniform wind case.

The analysis for best starting position was also repeated, and shows a high resemblance to the uniform wind results. This indicates that rough estimations or initial guesses can be derived from the uniform wind model, while a higher fidelity model can be used to detail the trajectories and better estimate power requirements as ABL effects become more critical under severe wind conditions.

In addition, the values of the objective function and total energy belonging to the best starting locations were compared between the two wind models. Both metrics are highly similar for low to moderate wind speeds, but show deviations up to 8% for higher wind velocities. These are also the situations in which the wind gradient is effectively exploited by the helicopter to improve its path performance.

Downdraft

The downdraft wind model adds localized aerodynamic complexity near the flight deck. This reveals to have significant impacts on the final approach phase. A main finding is that the helicopter's airspeed is mostly affected by the wind velocity deficit behind the hangar, but not by the downdraft strength. On the other hand, downdraft strengths have significant effects on the required power, thrust, and control effort in the final phase of the approach.

High wind speeds in combination with a strong downdraft could result in a premature reach of the power limit. This is because the power required increases significantly due to the downdraft, in the terminal approach phase just before initiating the landing. At the end of the trajectory, the power required with the downdraft model shows deviations of up to 80% from the power required in the case of the ABL wind models, as shown in Figure 12. The wind velocity deficit could even deteriorate the power requirement due to the decreased airspeed, also implying that the induced climb power is more dominant.

Although not included in this experiment, it is speculated that the decrease in airspeed could increase the control effort even further because of unsteady vortices and turbulence resulting from the ship's superstructure. The results suggest that an appropriate definition of SUOLs should account for these localized airflow effects.

CONCLUSIONS

A physics-based simulation framework has been developed and used to analyze optimal shipboard recovery operations of unmanned helicopters under performance and geometric constraints, for various wind conditions and starting positions.

Optimal paths exploit the wind and wind gradients to achieve extra ground speed in the initial phase or deceleration near the deck. The feasible approaches are considered practical for realistic maritime operations. The trajectories stay relatively consistent for different wind models at low to moderate wind speeds, but similarity values may drop for extreme cases. Clustering the optimal starting positions of the helicopter for given wind directions and speeds is therefore reasonable in the scope of providing operational guidelines.

The downdraft behind the hangar, for Northerly winds, has a substantial impact on the required power before the landing phase. This effect should be taken into account while determining SUOLs. The wind velocity deficit behind the hangar does not seem to yield significant results on the control effort or power required. However, the instant drop in airspeed could result in dangerous situations when including other local airflow effects such as turbulence or unsteady vortices.

Future work should be aimed at validating the optimized trajectories with higher-fidelity models or flight tests. Sensitivity studies on the helicopter's initial speed and distance to the ship could also be carried out. Variations in the objective function could be explored to evaluate different weighting factors for the time and control effort terms, to obtain energy-optimal trajectories. Lastly, the LCSS similarity score could also be used as an objective if one is interested, for operational reasons, in minimizing the deviation of a trajectory from a reference case.

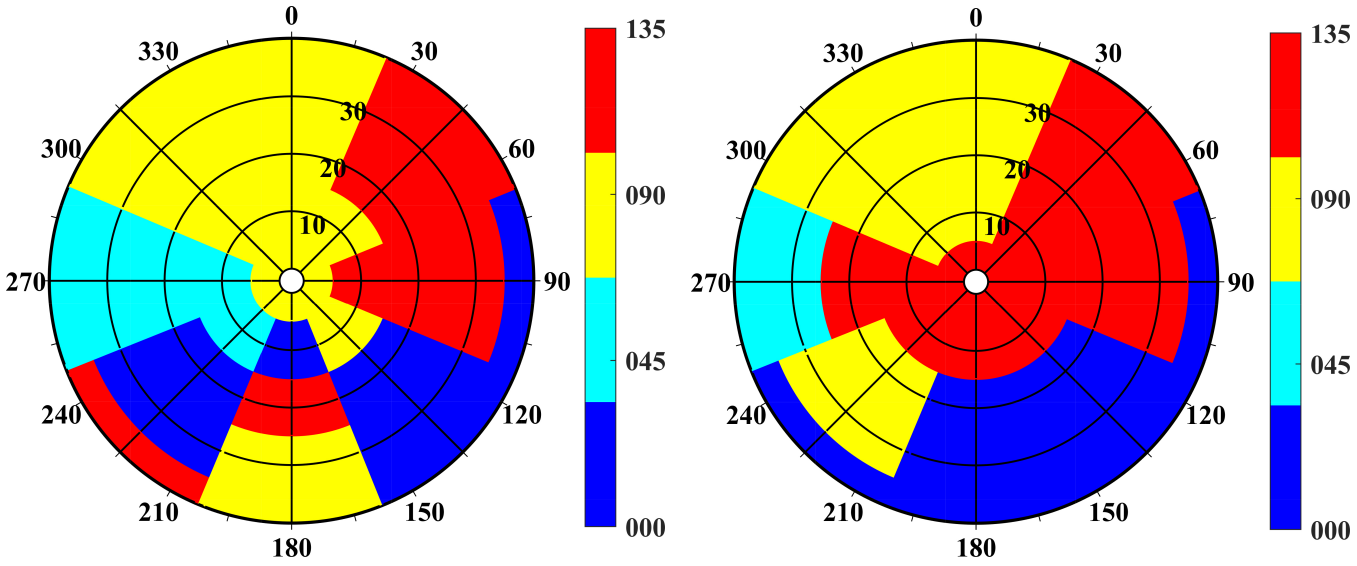

(a) Minimum objective function values

(b) Minimum energy required

Figure 11: Best starting positions for helicopter approach trajectories in uniform winds.

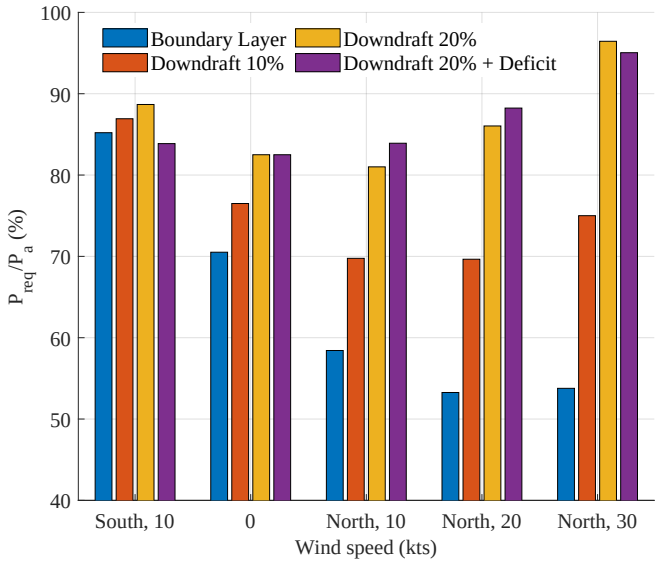

Figure 12: Power required at the end of the approach trajectories, as affected by the ABL wind model complemented by different downdraft strengths and velocity deficits.

REFERENCES

1. James S. Forrest, Ieuan Owen, Gareth D. Padfield, and Steven J. Hodge. Ship–helicopter operating limits prediction using piloted flight simulation and time-accurate airwakes. *Journal of Aircraft*, 49(4):1020–1031, 2012.

2. S.J. Tate. A dynamic challenge: Helicopter/ship interface simulation – development, integration and application. *Defence Research Agency - Flight Dynamics and Simulation Department*, pages 10.1–10.16, 1995. AGARD-CP-577, AGARD Flight Vehicle Integration Panel Symposium on 'Flight Simulation Where are the Challenges?', Braunschweig, Germany, May 1995.

3. M. Voskuijl, G.D. Padfield, D.J. Walker, B.J. Manimala, and A.W. Gubbels. Simulation of automatic helicopter deck landings using nature inspired flight control and flight envelope protection. *The Aeronautical Journal*, 114(1151):25–34, 1 2010.

4. Tri D. Ngo and Cornel Sultan. Model predictive control for helicopter shipboard operations in the ship airwakes. *Journal of Guidance, Control and Dynamics*, 39(3):574–589, 3 2016.

5. I. Owen, M.D. White, G.D. Padfield, and S.J. Hodge. A virtual engineering approach to the ship-helicopter dynamic interface – a decade of modelling and simulation research at the university of liverpool. *The Aeronautical Journal*, 121(1246):1833–1857, 12 2017.

6. W.A. Memon, I. Owen, and M.D. White. Simshol: A predictive simulation approach to inform helicopter–ship clearance trials. *Journal of Aircraft*, 57(5):854–875, 10 2020.

7. J.S. Forrest, S.J. Hodge, I. Owen, and G.D. Padfield. An investigation of ship airwake phenomena using time-accurate cfd and piloted helicopter flight simulation. *European Rotorcraft Forum*, 2008.

8. J.M.P. Figureira, A. Taghizad, and M. Abid. The use of simulation tools to estimate ship-helicopter operating limitations. *AIAA Aviation Forum*, 6 2017. AIAA Modeling and Simulation Technologies Conference.

9. James S. Forrest and Ieuan Owen. An investigation of ship airwakes using detached-eddy simulation. *Computers & Fluids*, 39(4):656–673, 2010.

10. N. Taymourtash, D. Zagaglia, A. Zanotti, G. Gibertini, and G. Quaranta. Wind tunnel investigation of a helicopter model in shipboard operations. *European Rotorcraft Forum*, 1:111–123, 2019.

11. C.H. Kääirä. *Investigating the Impact of Ship Superstructure Aerodynamics on Maritime Helicopter Operations*. PhD thesis, University of Liverpool, 2012.

12. A. Sharma, J. Xu, A. Padthe, P.P. Friedmann, and K. Duraisamy. Simulation of maritime helicopter dynamics during approachto landing with time-accurate wind-over-deck. 2019.

13. T.R. Fell, M.D. White, M. Jump, and I. Owen. Initial progress to establish flying qualities requirements for maritime unmanned aircraft systems. *European Rotorcraft Forum (ERF)*, 2014. Universities of Liverpool and Lincoln.

14. T.R. Fell, M.D. White, M. Jump, and I. Owen. Towards establishing flying qualities requirements for maritime unmanned aircraft systems. *Annual Forum Proceedings - AHS International*, 2:1465–1474, 01 2015.

15. T.R. Fell, M.D. White, M. Jump, and I. Owen. Progress in establishing scalable flying qualities requirements for maritime unmanned rotorcraft systems. *European Rotorcraft Forum (ERF)*, 2016. Universities of Liverpool and Lincoln.

16. T.M. Foster. Dynamic stability and handling qualities of small unmanned-aerial-vehicles, 2005. MSc thesis. Brigham Young University.

17. R.J.J. Bakker, M. Voskuijl, and D. Zilver. Simulation model and control system of the ph-1aa unmanned helicopter, 2023. NLR-CR-2023-118.

18. Commando Zeestrijdkrachten NLD and Bundesamt für Ausrüstung; Informationstechnik und Nutzung der Bundeswehr (BAAINBw) DEU. Technical arrangement to the memorandum of understanding between the federal ministry of defence of the federal republic of germany and the minister of defence of the kingdom of the netherlands concerning the cooperation in the field of research and technology on ship-deck environment and efficient drone operations (speedops), 2023.

19. P. Comeau, Alanna Wall, et al. Supporting shipboard helicopter flight testing with simulation and metrics for predicting pilot workload. *The Journal of Defense Modeling and Simulation*, 2022. SAGE Publications.

20. Koninklijke Marine. *Opereren met helikopters aan boord van CZSK-eenheden*. 2022.

21. D. Lee, J.F. Horn, L.N. Long, and N.S. Uzol. Simulation of helicopter shipboard launch and recovery with time-accurate airwakes. *Journal of Aircraft*, 42(2):448–461, 2005.

22. Z. Cai, Z. Hao, J. Zhao, and Y. Wang. Obstacle avoidance and tajectory tracking control of a quadcopter uav under wind conditions. *International Conference on Guidance, Navigation and Control*, pages 6053–6062, 2023.

23. Y. Zhao, A.A. Jhemi, and R.T.N. Chen. Optimal vertical takeoff and landing helicopter operation in one engine failure. *Journal of Aircraft*, 33(2):337–346, 1996.

24. H.G. Visser. Optimization of balanced field length performance of multi-engine helicopters. *AIAA*, pages 150–162, 2000.

25. S.F. Tang. Optimization of helicopter noise abatement arrival trajectories with the software tool noishhh, 2007. MSc thesis. Delft University of Technology.

26. D.J. Hendriks. Optimization of helicopter noise and emissions abatement departure procedures, 2013. MSc thesis. Delft University of Technology.

27. S. Hartjes. *An Optimal Control Approach to Helicopter Noise and Emissions Abatement Terminal Procedures*. PhD thesis, Delft University of Technology, 2015.

28. T. Tsuchiya, H. Ikaida, H. Ishii, H. Gomi, and Y. Okuno. Real-time trajectory optimization for noise abatement of helicopter landings. *Journal of Mechanical Systems for Transportation and Logistics*, 4(2):95–110, 2011.

29. H.G. Visser, M.D. Pavel, and S.F. Tang. Optimization of rotorcraft simultaneous non-interfering noise abatement approach procedures. *Journal of Aircraft*, 46(6):2156–2161, 2009.

30. I.C. Cheeseman and W.E. Bennet. The effect of the ground on a helicopter rotor in forward flight. *Aeronautical Research Council - Reports and Memoranda*, (3021), 1955.

31. J. Wieringa and P.J. Rijkoort. *Windklimaat van Nederland*. Staatsuitgeverij, Den Haag, 1983. Koninklijk Nederlands Meteorologisch Instituut - De Bilt. ISBN 90 12 044669.

32. J.C. Kaimal and J.J. Finnigan. *Atmospheric Boundary Layer Flows - Their Structure and Measurement*. Oxford University Press, 1994. ISBN 0-19-506239-6.

33. N.J. Cook. The deaves and harris abl model applied to heterogeneous terrain. *Journal of Wind Engineering and Industrial Aerodynamics*, 66(3):197–214, 1997.

34. S. A. Hsu and E. A. Meindle D. B. Gilhousen. Determining the power-law wind-profile exponent under near-neutral stability conditions at sea. *American Meteorological Society*, pages 757–765, 1994.

35. Y. Tominaga and M. Shirzadi. Wind tunnel measurement dataset of 3d turbulent flow around a group of generic buildings with and without a high-rise building. *Data in Brief*, 39, 2021.

36. David G. Hull. *Optimal Control Theory for Applications*. Mechanical Engineering Series. Springer New York.

37. Donald E. Kirk. *Optimal control theory: an introduction*. Dover Publications.

38. United States Army Aviation and Missile Command. Aeronautical design standard - performance specification handling qualities requirements for military rotorcraft, 5 1996. ADS-33E-PRF.

39. G. Guglieri and R. Celi. Some aspects of helicopter flight dynamics in steady turns. *Journal of Guidance, Control and Dynamics*, 21(3):383–390, 1998.

40. F. Xiang, T. Shen, and D. Li. Trajectory planning for mini unmanned helicopter in obstacle and windy environments. *Aircraft Engineering and Aerospace Technology*, 90(5):806–814, 2018. School of Aeronautic Science and Engineering, Beihang University.

41. Y. Tanabe and H. Sugawara. Aerodynamic validation of rflow3d code with uh-60a data including high advance ratios. *41st European Rotorcraft Forum*, 2015.

42. Y. Nie, O. Faqir, and E.C. Kerrigan. Iclocs2: Try this optimal control problem solver before you try the rest. In *2018 UKACC 12th International Conference on Control (CONTROL)*, pages 336–336, 9 2018.

43. M. Kelly. Transcription methods for trajectory optimization: a beginners tutorial. *arXiv: Optimization and Control*, 2 2015.

44. M. Diehl. *Lecture Notes on Numerical Optimization (Preliminary Draft)*. Department of Microsystems Engineering and Department of Mathematics, University of Freiburg, Germany, 3 2016.

45. Y. Tao, A. Both, R.I. Silveira, K. Buchin, S. Sijben, R.S. Purves, P. Laube, D. Peng, K. Toohey, and M. Duckham. A comparative analysis of trajectory similarity measures. *GIScience & Remote Sensing*, 58(5):643–669, 2021.

46. M. Vlachos, G. Kollios, and D. Gunopulos. Discovering similar multidimensional trajectories. In *Proceedings 18th International Conference on Data Engineering*, pages 673–684, 2002.

47. T. Górecki. Using derivatives in a longest common subsequence dissimilarity measure for time series classification. *Pattern Recognition Letters*, 45:99–105, 2014.